The dust and gas environment of comet 8P/Tuttle

Pedro J. Gutiérrez,[1⋆] Luisa M. Lara,[1] and Fernando Moreno[1]
[1]*Instituto de Astrofísica de Andalucía, CSIC, Glorieta de la Astronomía s/n, 18008 Granada, Spain*

Accepted XXX. Received YYY; in original form ZZZ

ABSTRACT

Comet 8P/Tuttle has been selected as a possible backup target for the Comet Interceptor mission (ESA). This comet was observed intensively during its previous perihelion passage, in January 2008. From those observations, important information was obtained about the physical properties of the nucleus and coma. The present study focuses on the coma of 8P/Tuttle using visible spectra and images to derive gas and dust production rates. The production rates obtained suggest that this comet can be considered as "typical" concerning the C_2/CN and C_3/CN ratios, although, depending on the criteria adopted, it could be defined as C_3 depleted. NH_2 production rates suggest an enrichment of this molecule. Visible and infrared images have been analysed using a Monte Carlo dust tail model. At comparatively large heliocentric distances, the coma is characterised by a dust-to-water ratio around or less than 1. Nevertheless, when the comet approaches perihelion, and the subsolar latitude crosses the equator, the coma dust-to-water ratio increases significantly, reaching values larger than 6. Such a high dust-to-gas ratio around perihelion suggests that the nucleus of 8P/Tuttle is also "typical" regarding the refractory content, considering the comparatively high values of that magnitude estimated for different comets.

Key words: Comets: general – Comets: individual: 8P – Methods: numerical

1 INTRODUCTION

Comet 8P/Tuttle (hereinafter 8P or Tuttle, indistinctly) was initially discovered by the french astronomer Méchain in January 1790. It was rediscovered again in January 1858 by H. P. Tuttle, and soon after, its periodic nature, and match with the comet of 1790, was clearly established. Since then, it is known that comet 8P revolves around the Sun with a period between 13 and 14 yr, presently 13.61 yr. Comet 8P was classically classified as a Jupiter-family comet (JFC) as its orbital period is less than 20 yr. Nevertheless, given its comparatively low Jupiter Tisserand invariant of 1.601[1], 8P must be classified as Halley-type comet according to the criterion by Carusi & Valsecchi (1987) and Levison & Duncan (1994) or, in the most general case, as nearly isotropic comet (e.g. Levison 1996), probably coming from the Oort cloud.

Observations of comet Tuttle have been reported for almost all perihelion passages since discovery. Nevertheless, the previous apparition (2007–2008) was particularly favourable for its observation because the comet passed at a record distance of 0.25 au from Earth. Most of our present and confident knowledge on this comet comes from that perihelion passage.

Regarding nucleus characteristics, some distant (at 6.29 au inbound) observations in the visible corresponding to the 1994 perihelion passage allowed Licandro et al. (2000) to estimate a nucleus radius of 7.3 km. During the following perihelion passage, that of 2008, and also from distant observations in the visible (at 7.42 au inbound), Snodgrass et al. (2008) derived an equally large size for the nucleus, obtaining a radius of 7.6 km. According to Groussin et al. (2019), Weissman et al. (2008) also estimated a large size for the nucleus of 8P, obtaining a radius of approximately 6 km, as previously, from observations at large heliocentric distances.

The close approach to Earth of comet 8P in 2008 allowed Harmon et al. (2008a, 2008b, 2008c) to characterise the nucleus from radar observations. These observations soon revealed that the nucleus of 8P was formed by two lobes with approximate diameters of 5.6 and 4.4 km (Harmon et al. 2008b). A detailed analysis of those radar observations was later given in Harmon et al. (2010). By fitting radar images with a shape model formed by two prolate spheroids, Harmon et al. (2010) estimated that the two lobes had dimensions of 5.75 x 4.11 km and 4.25 x 3.27 km, leading to an effective radius of 3.1 km if calculated from its projected area. Taking advantage of its close approach to Earth, 8P was also observed with the *HST* by Lamy et al. (2008). These authors concluded that the visible lightcurve was also best-fitted by considering a nucleus composed of two lobes. Assuming an albedo of 0.04, Lamy et al. (2008) estimated that the nucleus consisted of two spheres with radii 1.2 km and 2.8 km, leading to a mean radius of 3.0 km from the

⋆ E-mail: pedroj@iaa.es
[1] JPL Small-Body Database.
https://ssd.jpl.nasa.gov/sbdb.cgi?sstr=8P&orb=1

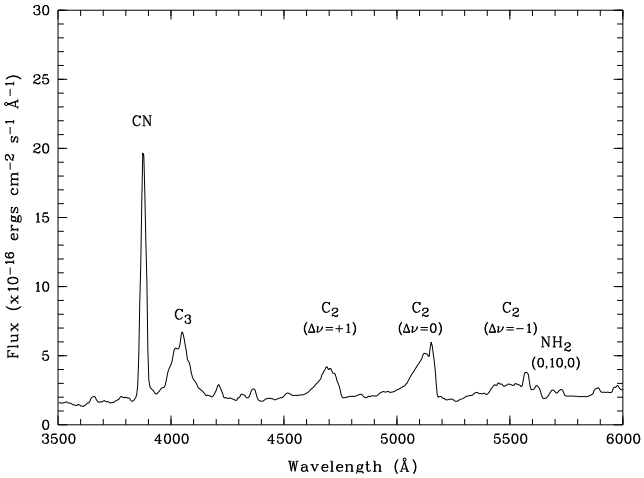

Figure 1. Spectrum of 8P/Tuttle on 15 December 2007 after averaging the cometary emission at $-4600 \leq \rho \leq 4600$ km, where ρ stands for cometocentric distance as projected on the plane of the sky, and negative and positive values denote the north and south directions, respectively.

equal projected area. This estimate is in agreement with the size derived from radar observations. During the 2007–2008 apparition, comet 8P was also observed in the infrared with *Spitzer* by Groussin et al. (2019). These authors studied the 24 m infrared emission of 8P considering the slightly different results on the shape (prolate shapes vs spheres for the two lobes) and constraints on the spin axis orientation from Harmon et al. (2010) and Lamy et al. (2008). Groussin et al. (2019, table 3) summarise the differences in the characterisation of the nucleus of 8P from the observations by Lamy et al. (2008) and Harmon et al. (2010), including the derived spin axis orientations compatible with each observation. From their detailed and careful analysis, Groussin et al. (2019) concluded that the thermal emission was best reproduced by the *HST* main results, refining the size of the nucleus, i.e. a bilobate nucleus formed by two spheres with radii 1.1 ± 0.1 and 2.7 ± 0.1 km and a spin axis orientation of (RA, Dec) = $(285 \pm 12, +20 \pm 5)°$. By combining their size estimate with the *HST* magnitude, Groussin et al. (2019) determined that the R geometric albedo of 8P was 0.042 ± 0.008.

Regarding the spin period of the nucleus, Lamy et al. (2008) and Harmon et al. (2010) obtained a very similar value around 11.4h. Half that spin period has been favoured by Waniak et al. (2009) (as well as by Woodney et al. 2008) from their analysis of the repeatability and kinematics of CN shells. Nevertheless, the authors recognised that their analysis was based on a simplified model and that the 11.4 h period could be confirmed from CN structures with more sophisticated modelling.

Volatile production rates were also subject of intensive study (e.g. Biver et al. 2008, Crovisier et al. 2008, Barber et al. 2009, Lovell & Howell 2008, Bonev et al. 2008, Lippi et al. 2009, Bockelée-Morvan et al. 2008, Kobayashi et al. 2010, Böhnhardt et al. 2008, Jehin et al. 2009, Schleicher & Bair 2008, Borisov et al. 2008, etc.) during the last closest approach to Earth and near perihelion by using different techniques and telescopes. These studies made it possible to estimate the water production rate around perihelion, being within the range of 1 to 6×10^{28} mol sec^{-1}. Likewise, the production rates of different molecules (CO, HCN, C_2H_2, CH_4, C_2H_6, CH_3OH, CN, C_3, and C_2) were also obtained. Observations also suggested that 8P could have a low dust-to-gas ratio (e.g. Schleicher 2007a). Some discrepancies exist concerning the singularity of this comet. On the one hand, Bonev et al. (2008) and Böhnhardt et al. (2008) concluded that the mixing ratios of parent molecules in 8P were unusual (with a strong enrichment of methanol and being depleted in other molecules), suggesting that the two lobes could have different volatile composition. On the other, Kobayashi et al. (2010) obtained that the relative abundances of 8P, even if depleted in some molecules with regard to Halley-type comets, were not atypical when compared to long-period comets, finding no evidence of chemical heterogeneity in their observations. Regarding daughter molecules, a typical composition has been reported (e.g. Schleicher 2007a).

Knowledge of 8P is very valuable for the planning of the future *Comet Interceptor* (hereinafter CI) mission. CI is an ESA F-class mission expected to be launched in 2028 (Snodgrass & Jones 2019) and aimed at exploring a dynamically new comet. The mission is being designed and will be launched without a specific main target. The spacecraft will travel up to the L2 Lagrangian point where it will wait in hibernation until a suitable target is found. In the event of an appropriate target not being discovered before CI had to leave L2, several comets have been selected as scientific valuable backup targets for the mission (Schwamb et al. 2020). Comet 8P/Tuttle is presently considered as a potential backup target for CI. The CI team encouraged the community to observe those comets and analyse archival data in order to assist its scientific prioritisation (Schwamb et al. 2020), and the safe and scientifically fruitful flyby of the spacecraft if finally one of those comets is selected as target. Among the selected backup comets, 8P is the only one probably coming from the Oort cloud, which makes it particularly interesting.

Comet 8P was again at its perihelion (the last one before CI launching) in late August 2021. Nevertheless, its observability was poor given the low solar elongation. This unfortunate circumstance makes all the data and information already available on this comet of great importance. All the above studies provide the community with invaluable knowledge on comet 8P, particularly regarding the characteristics of the nucleus and the volatile composition of the coma. Information regarding the refractory component is still scarce. In this work, we focus on the gas and dust characteristics. In the next section, a summary of our observations is presented. Section 3 is devoted to our spectroscopic observations, aimed at deriving gas productions rates in the visible. In Section 4, images in the visible, together with archived images taken in the infrared with *Spitzer* under the program ID 40270 (PI O. Groussin), are analysed by using a Monte Carlo model to derive dust characteristics and production rates. In Section 5, the main results on both gas and dust are discussed.

Table 1. Summary of observations of 8P considered in this study. Infrared images are obtained from the *Spitzer Heritage Archive* from the program developed by O. Groussin as described in the text. Details on the characteristics of the grisms are given in the text.

Date	Instrument @Telescope	Filter Grism	Pixel Scale [arcsec/pixel]	r_h [au]	Δ [au]	Phase [°]
15 Dec 2007	CAFOS@2.2-m	*R*-Cousins B200	0.53	1.21	0.40	47.7
4 Jan 2008	ALFOSC@NOT	*R*-Bessell #3	0.21	1.08	0.26	61.3
22 June 2008	MIPS@*Spitzer*	24 m	2.45	2.25	1.58	23.4

Table 2. Emission and continuum bands extracted from the spectra as well as g-factors used to calculate column densities. For CN, the two given g-factors were calculated, as described in the text, for the two observing dates, 15 December 2007, and 4 January 2008, respectively. For the rest of the molecules, a constant g-factor was considered.

Spectral region Å	Species	Left-hand cont. Å	Right-hand cont. Å	g-factor ergs s^{-1} mol^{-1}
3830–3905	CN	3700–3815	3910–3970	3.258×10^{-13} // 3.589×10^{-13}
3975–4150	C_3	3910–3970	4155–4190	1.452×10^{-12}
5375–5667	$C_2(\Delta\nu=-1)$	5220–5250	5769–5790	2.053×10^{-13}
5673–5766	NH_2	5653–5670	5769–5790	1.368×10^{-15}

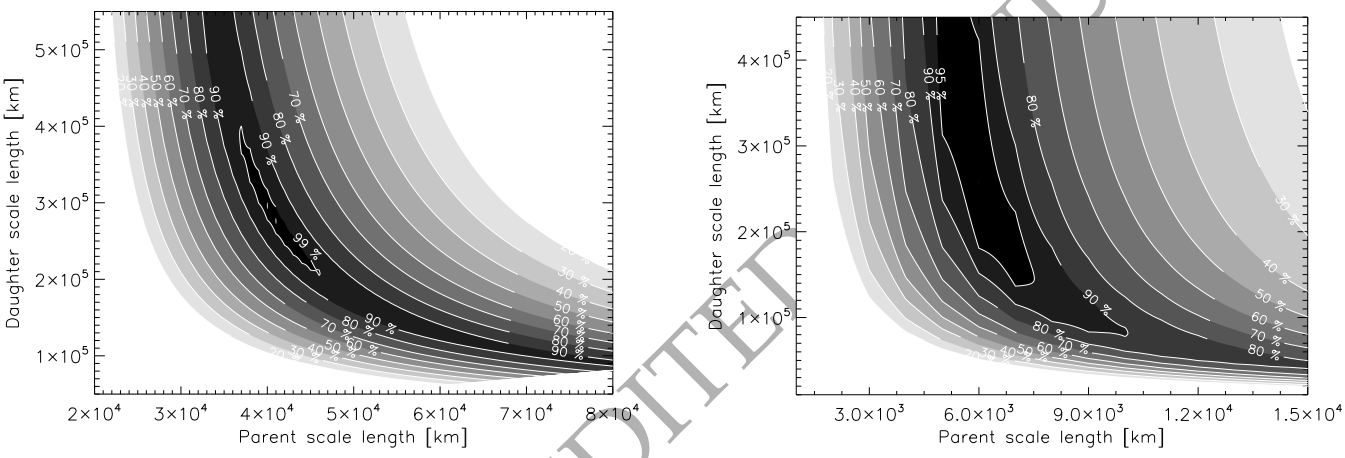

Figure 3. Confidence levels contours defined from the chi-square distribution obtained with the best-fitting production rate as a function of the parent and daughter scale lengths. The left panel corresponds to CN on 15 December 2007 in the North direction. This figure exemplifies a case in which the 99 per cent confidence region is well constrained. The Haser profiles with the best-fitting parameters, including errors, are shown in the upper left of Fig. 5. The right panel corresponds to C_3 on 15 December 2007 in the North direction. This figure exemplifies a case in which the daughter scale length is not well constrained, and the chi-square slightly drifts towards smaller values as l_d increases. As described in the text, in those cases, the 95 per cent confidence region is considered to define Q, l_p, and their corresponding uncertainties. The corresponding Haser profiles are displayed in the lower left of Fig. 5.

2 OBSERVATIONS AND DATA REDUCTION

8P was observed on 15 December 2007 from Calar Alto observatory (Spain) using the 2.2-m telescope equipped with the CAFOS instrument. On that night, several images through the Cousins *R*-filter as well as medium-resolution spectra with grism B200 were acquired. The grism B200 provides us with an observable spectral range between 328 and 843 nm with a wavelength scale of 0.447 nm per pixel and a spectral resolving power of 225 (at 500 nm). The slit of the spectrograph is oriented along the north-south and east-west directions, as projected on the plane of the sky, giving dust and gas radial profiles in those directions to study the deviations from isotropic gas and dust emission. For absolute calibration, observations of appropriate spectrophotometric standard stars were acquired. For the comet observations, the slit width is 2.5 arcsec whereas the usable selected length is 10.6 arcmin, which provides us with radial profiles along selected directions up to projected cometocentric distances of $\sim 10^5$km along both directions. The spectrophotometric standard star was observed with a width of 5 arcsec and the same slit length.

During and shortly after its closest approach to Earth, a second run to observe 8P was developed from El Roque de los Muchachos Observatory (Spain) with the ALFOSC instrument attached to the NOT telescope. Unfortunately, either technical problems or non-photometric conditions prevented us to scientifically use most of the observing time.

8P was successfully observed in this second run on the night of 4 January 2008. Broad-band images were taken through the Bessell *R*-filter and spectroscopic measurements were obtained with grism #3 with initial and final wavelengths of ~ 300 and 670 nm, respectively, a spectral resolution of 0.23 nm per pixel and a spectral resolving power of 190 (at 500.0 nm). The slit, of 2.5 arcsec of width and 6.3 arcmin length, was positioned along the N–S direction. Tracking on the comet was used and corresponding bias, flats, lamp spectra as well as calibration stars were also taken to perform standard calibration.

The spectra were reduced using the ESO-MIDAS standard reduction context *long* for long-slit spectra. The spectra were bias subtracted, flatfielded, wavelength calibrated, extinction corrected (using the standard extinction curve for both observatory sites), and flux calibrated. Since the spectrum of 8P/Tuttle covers the entire length of the slit, it is not possible to extract the sky contamination directly from the spectrum itself. Instead, this subtraction has been estimated from spectral regions free of gas emissions nearby the CN, C_2, C_3, and NH_2 bands. More details on the images and spectra reduction and calibration can be found in Lara et al. (2001, 2004a, 2004b) and Bertini et al. (2009).

Table 1 summarises observations as well as comet geometrical circumstances. Our observations were aimed at retrieving production rates of CN, C_2, C_3, and NH_2 and at determining dust properties and production rate using Monte Carlo models as described in e.g. Moreno et al. (2016). As our images were close in time, and the performance of Monte Carlo models may benefit from distant observations, we decided to include publicly available data in our study. On the one hand, our Afρ determined from the spectroscopic measurements in clear dust continuum regions were combined with amateur determinations of the Afρ parameter as a function of the heliocentric distance to constrain the dust model, as described in section 4. On the other hand, considering the recent publication by Groussin et al. (2019) and the suitability of including infrared observations in our Monte Carlo study, images of 8P available at the *Spitzer Heritage Archive*[2] corresponding to the program with ID 40270[3], PI: O. Groussin, were used. In particular, we utilised MIPS level 2 24-m images[4] taken on 22 June 2008, when the comet was at 2.25 and 1.58 au from the Sun and *Spitzer*, respectively. Shadow observations, showing consistency with the background sky, were subtracted from the mosaicked images to extract comet flux.

3 THE GAS COMA

The spectra of the comet are used to investigate the CN, C_2, C_3, and NH_2, in the directions probed by the slit. The spectral regions are specified in Table 2. For the subtraction of the underlying continuum in the gas emission bands, we have measured the continuum bordering each emission band (see Table 2) and approximated the continuum contribution to the band by interpolating the left- and right-hand continua (Lara et al. 2001). The conversion of the emission band fluxes into column densities makes use of constant g–factors for C_2, C_3, and NH_2 (Cochran et al. 1992, A'Hearn et al. 1995, Schulz et al. 1998), whereas the g–factor of the CN molecule is calculated for the heliocentric distance and velocity of 8P on every date from the set of values given by Schleicher (2010). Considering all the procedures involved, our estimate of the error in column densities determination is less than 5 per cent, at least up to moderate cometocentric distances (~ 5000 km). The outflow velocity of the gas adopted in this study is $v = 0.85\ r_h^{-0.5}$ (e.g. Cochran et al. 2012), where r_h is the heliocentric distance.

The gas profiles are asymmetric in the directions probed by the slit, indicating a non–isotropic gas emission. To obtain the production rates, Q, we used the Haser model (Haser 1957). We performed fits of the column density profiles, N, as a function of the projected cometocentric distance, ρ. Specifically, we fitted $log\ N - log\ \rho$ profiles in the E-W and N-S directions on 15 December 2007, and in the N-S direction on 4 January 2008. By considering the standard scale lengths given in Cochran et al. (1992), A'Hearn et al. (1995), and in Schulz et al. (1998), we produced theoretical column density profiles for each species by varying the production rate Q until the best match between observations and theoretical predictions is achieved. However, the parent and daughter scale lengths (l_p, l_d) do not satisfactorily fit the observed $N(\rho)$ regardless of the Q value (some examples are shown in Fig. 5). In general, the observed CN, C_3, and C_2 column density profiles versus projected cometocentric distance are noticeably flatter than the results of the Haser modelling with classical parent and daughter scale lengths. This fact points to an l_p, or l_d or both larger than the standard values. Only slightly better results are obtained if the standard scale lengths are corrected for heliocentric distance by using a power law index of 1.5 (subtracting our heliocentric dependence of the outflow velocity to the theoretically expected increase of the photodissociation rates).

Therefore, to retrieve more confident production rates, both parent (l_p) and daughter (l_d) scale lengths have to be fitted as well. Given the dispersion of the column densities profiles (see examples in Fig. 5), to estimate the best-fitting parameters, their significance, and errors bars, the following procedure, inspired by the work performed by Fray et al. (2005) or Langland-Shula & Smith (2011), among others, has been implemented. Column densities have been first binned in a cometocentric logarithmic scale. The error bar for each bin is defined by comparing the 5 per cent of the median with the standard deviation of the data included in the bin, and choosing the larger of the two quantities. Then, a grid of plausible parent (l_p) and daughter (l_d) scale lengths is defined, and the cometocentric Haser profile for each (l_p, l_d) pair is calculated. The cometary gas production rate, Q, is then obtained by scaling all those profiles to minimise the chi-square between the theoretical and observational column densities. This allows to obtain a map of the chi-square (see examples in Fig. 3) as a function of both scale lengths and to build the corresponding chi-square distribution, which is used to estimate confidence regions. Values and errors of the best-fitting parameters are defined as the medians and stan-

[2] https://sha.ipac.caltech.edu/applications/Spitzer/SHA/
[3] Title: "Measuring the physical properties of the nucleus of 8P/Tuttle."
[4] PBCD –post basic calibrated data– obtained from combining individual data frames taken according to the original program processed with the *Spitzer Science Center* pipeline version S18.13.0

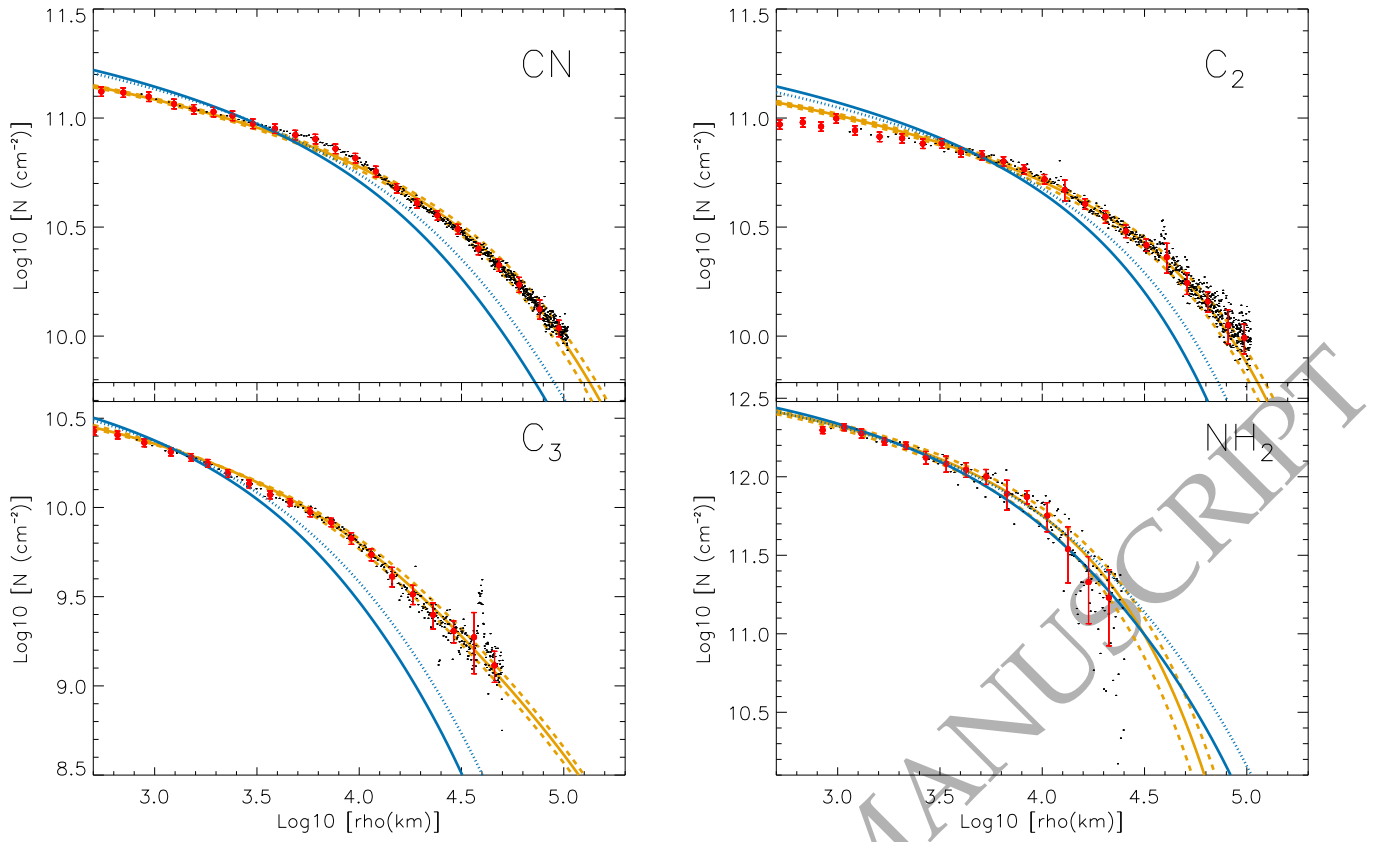

Figure 5. Column density radial profiles (dots) for the four different molecules on 15 December 2007 in the North direction. Red solid circles with errors bars represent the data binned as described in the text. These latter data points are those fitted by a Haser profile. Orange solid line corresponds to the best achievable Haser fit with (l_p, l_d, Q) derived in this work. Orange dashed lines represent the corresponding profiles when errors are considered. The fits obtained with standard scale lengths are also shown as blue curves (the solid line corresponds to the uncorrected case and the dotted line to the corrected one for heliocentric distance). It can be seen that those profiles for CN, C_2, and C_3 are considerably steeper than observations. The values of scale lengths and productions rates are shown in Table 3.

dard deviations, respectively, of the parameters within the region of the 99 per cent of confidence, i.e. the sets of parameters that have a probability of less than 1 per cent of finding another set with a smaller chi-square.

The region of the 99 per cent of confidence is well constrained for most of the observational column densities (see, as an example, the left panel of Fig. 3). Nevertheless, some column densities do not allow to define the daughter scale length appropriately. The chi-square slightly drifts towards smaller values when the daughter scale length increases around a nearly constant parent scale length. This circumstance indicates that either the quality of the data is not sufficient, or the Haser model does not describe the underlying physics adequately, or both. An example of the chi-square confidence intervals when the daughter scale length cannot be constrained is shown in the right panel of Fig. 3. In these circumstances, we have verified that a change of a factor of ~ 2 in the daughter scale length implies a variation of the chi-square of the order of ~ 1 per cent or less. Fortunately, that circumstance, i.e. a poorly constrained daughter scale length, has a limited impact on the retrieved production rate. In regions with high confidence levels, the production rate best-fitting the data is controlled mainly by the parent scale length. Thus, in those cases, a confidence region of 95 per cent is used to determine the best-fitting parameters and their corresponding errors. The level of 95 per cent of confidence is admittedly arbitrary but, given the aforementioned slow drift of the chi-square, smaller confidence values may artificially increase the error bars with poorer representations of the data. As previously described, within the 95 per cent confidence region, most of the dispersion of the Q values is due to the variation of the parent scale length within the region, regardless of the daughter scale length. Best-fitting parameters and errors defined from median values and standard deviations in the confidence region may introduce a bias, which depends on the upper limit of the daughter scale length. In order to reduce the bias introduced by the drift of the chi-square when the daughter scale length increases (which also favours smaller parent scale lengths and production rates), just in these circumstances, Q and l_p are defined as the mean of the maximum and minimum values found within the 95 per cent confidence region, and the corresponding errors are calculated as half the distance between the maximum and the minimum. In these cases, l_d is left unconstrained.

The sets of l_p, l_d, and Q, and corresponding errors, that allow a good fit to the observations are listed in Table 3. Only a lower limit, obtained from the 95 per cent confidence

Table 3. Gas production rates, Q, of different molecules, and the best-fitting parent and daughter scale lengths (l_p, l_d) in the coma of 8P/Tuttle. For comparison, although the fit to observations is not optimal, the production rates obtained using standard (l_p, l_d), both uncorrected and corrected for heliocentric distance as described in the text, are also listed. Those latter data are identified with "st" at the corresponding line, and the solutions for the uncorrected and corrected scale lengths are separated by "//"

Species	Direction	15 Dec 2007			4 Jan 2008		
		l_p (10^3km)	l_d (10^4 km)	Q (10^{25}s^{-1})	l_p (10^3 km)	l_d (10^4km)	Q (10^{25}s^{-1})
CN	N	40.0 ± 2.2	29.4 ± 4.7	5.3 ± 0.3	27.0 ± 2.0	> 38.5	5.8 ± 0.4
	S	59.0 ± 11.1	14.0 ± 4.0	7.7 ± 1.4	37.5 ± 6.5	> 22.8	9.2 ± 1.5
	E	63.0 ± 11.0	14.7 ± 3.8	8.4 ± 1.5			
	W	28.0 ± 3.0	> 29.2	4.0 ± 0.4			
	Avg			6.3 ± 0.9			7.5 ± 0.9
st	N	13//17.3	21//28.0	2.5//3.0	13//14.6	21//23.6	3.9//4.1
st	S	"	"	2.6//3.0	"	"	4.7//5.0
st	E	"	"	2.6//3.1			
st	W	"	"	2.5//3.0			
st	Avg			2.6//3.1			4.3//4.6
C_2	N	75.0 ± 6.0	9.9 ± 1.0	8.2 ± 0.7	34.0 ± 16.0	> 4.8	7.2 ± 3.1
	S	75.0 ± 7.0	10.1 ± 1.1	8.1 ± 0.7	45.5 ± 19.5	> 4.8	9.1 ± 3.7
	E	88.0 ± 5.7	10.9 ± 0.8	9.3 ± 0.6			
	W	65.0 ± 8.3	10.5 ± 1.9	6.8 ± 0.9			
	Avg			8.1 ± 0.7			8.2 ± 3.4
st	N	22//29.3	6.6//8.8	3.4//4.0	22//24.7	6.6//74.3	5.5//5.8
st	S	"	"	3.4//4.0	"	"	5.9//6.2
st	E	"	"	3.5//4.1			
st	W	"	"	3.2//3.8			
st	Avg			3.4//4.0			5.7//6.0
C_3	N	6.0 ± 1.0	> 14	0.23 ± 0.02	4.0 ± 0.7	4.1 ± 1.1	0.35 ± 0.04
	S	5.5 ± 0.5	> 25	0.22 ± 0.01	4.0 ± 0.7	4.9 ± 1.3	0.38 ± 0.05
	E	5.5 ± 0.5	> 16	0.23 ± 0.02			
	W	5.0 ± 1.0	> 25	0.20 ± 0.01			
	Avg			0.22 ± 0.01			0.37 ± 0.05
st	N	2.8//3.7	2.7//3.6	0.16//0.19	2.8//3.2	2.7//3.0	0.28//0.31
st	S	"	"	0.17//0.20	"	"	0.30//0.32
st	E	"	"	0.19//0.21			
st	W	"	"	0.17//0.19			
st	Avg			0.18//0.20			0.29//0.31
NH_2	N	14.0 ± 1.6	2.1 ± 0.3	48.6 ± 5.3	5.0 ± 3.7	> 2.5	40.2 ± 8.6
	S	15.0 ± 1.5	2.2 ± 0.3	43.2 ± 4.2	17.0 ± 1.7	2.4 ± 0.3	87.7 ± 8.7
	E	5.5 ± 0.3	7.7 ± 1.5	20.1 ± 1.1			
	W	18.0 ± 1.2	2.3 ± 1.9	50.3 ± 3.4			
	Avg			40.6 ± 3.5			63.9 ± 8.6
st	N	5.3//7.1	6.2//8.3	21.9//25.3	5.3//6.0	6.2//7.0	33.8//36.1
st	S	"	"	17.9//21.5	"	"	34.6//37.0
st	E	"	"	19.9//23.5			
st	W	"	"	18.0//21.7			
st	Avg			19.4//23.0			34.2//36.6

region, is given for l_d when it is unconstrained. These cases are generally characterised by large error bars both in Q and l_p, although they are usually not larger than 20 per cent of the nominal value. The worst case is C_2 on 4 January 2008, in which the errors are estimated somewhat below 50 per cent. To facilitate comparison, Table 3 also shows production rates derived for standard (l_p, l_d), both uncorrected and corrected for heliocentric distance. Fig. 5 shows the gas column density radial profiles observed on 15 December 2007 in the N direction together with the Haser fit using the standard (l_p, l_d) and those retrieved in this work. Table 4 lists the log [Q(C_2)/Q(CN)], log [Q(C_3)/Q(CN)], log [Q(NH_2)/Q(CN)] and also log [Afρ/Q(CN)] obtained from our study. As the gas production rates are determined for several slit directions, we have averaged them before calculating the ratios.

The best-fitting procedure results in averaged Q values for CN, C_2, and NH_2 that are significantly larger (more than a factor 2) than those derived using standard scale lengths on 15 December 2007 (r_h = 1.21 au). This difference becomes smaller on 4 January 2008 (r_h = 1.08 au), when the best-fitting procedure yields production rates for CN, C_2, and NH_2 that are 74, 44, and 87 per cent, respectively, larger than those obtained with standard scale lengths. Differences

for C_3 are significantly smaller, being ~25 per cent on both dates. When the standard scale lengths are corrected for heliocentric distance, differences diminish, but they are still significant.

Asymmetries in production rates along the directions probed by the slit are seen for most molecules. On 15 December 2007, NH_2 shows the highest asymmetry, ranging from 6 to 50 per cent of the average value. CN and C_2 display more moderate asymmetries, with values between 16 and 37 per cent for the former, and between 0 and 16 per cent for the latter. C_3 shows a low asymmetry, with values ranging from 1 to 10 per cent. On 4 January 2008, asymmetries tend to reduce. NH_2 displays a 37 per cent of asymmetry, CN a 22 per cent, C_2 a 12 per cent, and C_3 a 4 per cent. Asymmetries for CN and C_2 are similar to those obtained by Jehin et al. (2009) at perihelion, about four weeks after our last observation. The main difference is found in C_3. In our case, this molecule shows the lowest asymmetry, while Jehin et al. (2009) obtained a ~30 per cent. Given the different slit orientations (Tail-Sun in Jehin et al. 2009), a direct comparison of the asymmetries seems difficult.

In order to compare our best-fitting scale lengths with those available in the literature, they must be converted to a common heliocentric distance. Scale lengths are generally assumed to follow a power law of the heliocentric distance, r_h, i.e. ${r_h}^{\alpha}$. Presently, different α indexes have been retrieved from various observational datasets, frequently showing discrepancies when the same molecule is considered (see e.g. Rauer et al. 2003; Langland-Shula & Smith 2011). This fact shows the complexity of the physicochemical evolution of the coma. Theoretically, if the impact of coma dynamics is minimised, an $\alpha = 2$ is expected due to the dependence of the solar radiation on heliocentric distance. As in our study, an expansion velocity which depends on the heliocentric distance as ${r_h}^{-0.5}$ is considered, scale lengths may be approximately transformed to 1 au using $\alpha = 1.5$. Averaging the values retrieved for the different slit orientations (when l_d is constrained) and assuming $\alpha = 1.5$, all results are within the compilation of scale lengths given in Langland-Shula & Smith (2011, their table 10), except the daughter scale length of CN. Our average daughter scale length of CN on 15 December 2007 would be $l_d = (19.4 \pm 4.2) \times 10^4$ km, i.e. $(14.6 \pm 3.2) \times 10^4$ km at 1 au. This length is smaller than the lower limit of 19.9×10^4 km for l_d at 1 au of the CN scale lengths compiled by Langland-Shula & Smith (2011). Actually, our nominal value at $r_h = 1.21$ au is already slightly under that lower limit for $r_h = 1$ au. Given our large error bar, the discrepancy could be marginally explained by the chosen heliocentric dependence because a value of $\alpha = 1.5$ may be excessive based on the results by Langland-Shula & Smith (2011). These authors found that the heliocentric dependence of the l_d of CN may be characterised by an uncertain but shallow slope of 0.6 ± 0.5. Thus, in principle, our values for the l_d of CN could be marginally compatible with those found in the literature if a very low slope is considered to transform them to 1 au. Nevertheless, it is also possible that CN in comet 8P, when described by Haser modelling, actually pushes down the lower limit for l_d generally found in the literature. Jehin et al. (2009), on 28 January 2008, when the comet was at perihelion, obtained a value of $l_d = 16 \times 10^4$ km, already under the lower limit of the compilation by Langland-Shula & Smith (2011), as in our case. If that value is transformed to 1 au with our $\alpha = 1.5$, we would obtain an $l_d = 15.3 \times 10^4$ km, compatible with our $(14.6 \pm 3.2) \times 10^4$ km, within the error bar.

Table 4. Gas production rates quotients and the Afρ/Q(CN) obtained by averaging the $Q's$ in the N–S and E–W directions computed with (l_p, l_d) providing the best-fitting.

Ratio	15 Dec 2007	4 Jan 2008
log [$Q(C_2)/Q(CN)$]	0.11 ± 0.10	0.04 ± 0.23
log [$Q(C_3)/Q(CN)$]	-1.46 ± 0.09	-1.31 ± 0.11
log [$Q(NH_2)/Q(CN)$]	0.81 ± 0.10	0.93 ± 0.11
log [Afρ/Q(CN)]	-23.77 ± 0.08	-23.71 ± 0.07

4 THE DUST MODEL

The available observations to fit with the model are the CAFOS and ALFOSC images, on 15 December 2007, and 4 January 2008, respectively, the *Spitzer*/MIPS 24-m image on 23 June 2008, and the Afρ observations by CAFOS, ALFOSC, and CARA[5] and Cometas_Obs[6] amateur teams, all converted to R-band photometry using an aperture of ρ=10^4 km.

To retrieve the physical parameters of the dust from the observations, we used our Monte Carlo dust tail code. This code has been already used to characterise the dust environment in several dust-emitting objects, including comets and active asteroids (for recent applications of the model, see e.g. Moreno et al. 2019; de León et al. 2020). This model simulates a dust tail from a comet, or an active asteroid, by adding up the individual contribution to the brightness of each particle ejected from the parent nucleus. The particles, after leaving the object's surface and at a distance where they become decoupled from the gas drag (some 20 nuclear radii, R_n), move mainly under the influence of the Sun's gravity and solar radiation pressure. The nucleus gravity force is neglected, an approximation valid for small-sized nuclei, such as 8P. In such conditions, the trajectory of the particles becomes Keplerian, and their orbital elements are functions of their physical properties and velocities when the dust becomes decoupled from the gas (e.g. Fulle 1989). To build up sufficiently populated synthetic images with the Monte Carlo procedure, we usually launch from 2×10^6 to 10^7 particles for each observation date. Since the computing time of each Monte Carlo run is proportional to the dimensions of the image to be simulated, the CAFOS and ALFOSC images have been rebinned by factors of 4 and 8, resulting in pixel sizes of 616.7 and 321.5 km px^{-1}, respectively.

The ratio of radiation pressure force to the gravitational force exerted on the particles is given by the parameter β, defined as

$$\beta = \frac{F_{rad}}{F_{grav}} = C_{pr} Q_{pr} / (2\rho r) \quad (1)$$

In the previous expression, ρ is the particle density, and r is

[5] Cometary ARchive for Afrho, http://cara.uai.it/
[6] http://www.astrosurf.com/cometas-obs/

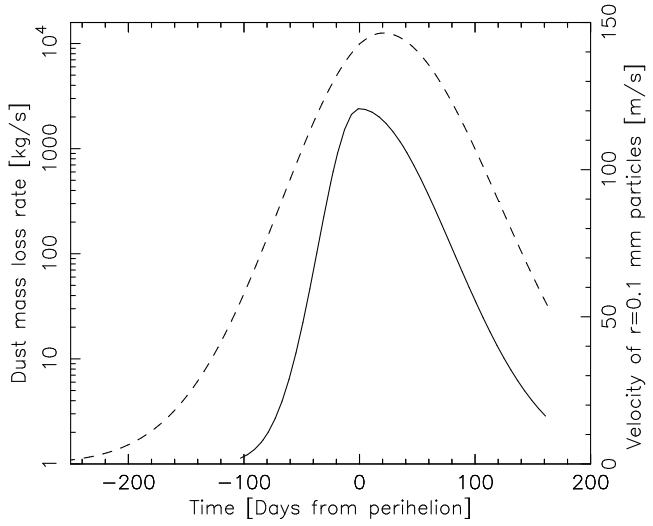

Figure 6. The speed of particles of 0.1 mm of radius once decoupled from the gas drag (solid line), and the dust mass loss rate (dashed line), as a function of time.

the radius of the particle. $Q_{\rm pr}$ is the scattering efficiency for radiation pressure, here taken as 1, as it converges to that value for absorbing spherical particles of radius $r \gtrsim 1$ m from Mie theory (see e.g. Moreno et al. 2012, their fig. 5). Finally, $C_{\rm pr}$ is the radiation pressure coefficient, which is computed as:

$$C_{\rm pr} = \frac{3Q_{\rm pr}E_\odot}{8\pi c G \mathrm{M}_\odot} = 1.19\times10^{-3}\ \mathrm{kg\ m^{-2}} \qquad (2)$$

where $E_\odot$ is the total solar radiation, c is the speed of light, G is the gravitational constant and $\mathrm{M}_\odot$ is the mass of the Sun.

The brightness, m, of a particle of radius r, expressed in mag arcsec^{-2}, is computed from the expression:

$$\pi r^2 = \frac{2.24\times10^{22}\pi {r_{\rm h}}^2\Delta^2 10^{0.4(m_\odot - m)}}{10^{-0.4\alpha\phi(\alpha)}} \qquad (3)$$

where $r_{\rm h}$ is the comet heliocentric distance in au, Δ is the Earth-to-comet distance in au, α is the phase angle, $\phi(\alpha)$ is the linear phase coefficient, and $m_\odot$ is the magnitude of the Sun in the corresponding red bandpass filter.

For the simulations of the *Spitzer*/MIPS 24-m image, we computed the particle flux using the equation:

$$F_\lambda = \frac{r^2}{{\Delta_{\rm S}}^2}\epsilon(\lambda,r)\pi B_\lambda[T(r_{\rm h})] \qquad (4)$$

where λ is the wavelength, ϵ is the grain emissivity, B_λ is the Planck function, $T(r_{\rm h})$ is the particle equilibrium temperature, and $\Delta_{\rm S}$ is the *Spitzer*-to-comet distance. The *Spitzer* heliocentric coordinates at the time of the June 2008 observation are obtained from the JPL Ephemeris. The equilibrium temperature can be computed by the balance between the absorbed solar and emitted thermal radiation as:

$$T(r_{\rm h}) = 278.8\left(\frac{1-A_{\rm B}}{\epsilon}\right)^{1/4}\frac{1}{\sqrt{r_{\rm h}}} \qquad (5)$$

In this equation, $A_{\rm B}$ is the Bond albedo. The dust grain temperature at 1.6 au has been estimated at 258 ± 10 K by Groussin et al. (2019). Hence, the quantity $\left(\frac{1-A_{\rm B}}{\epsilon}\right)^{1/4}$=1.17, so that the grain equilibrium temperature is computed as $T(r_{\rm h}) = 326.2/\sqrt{r_{\rm h}}$.

Given the large number of free parameters in the model, some assumptions must be made to make the problem tractable. Thus, the particle density is assumed at $\rho_{\rm p}$=800 kg m^{-3}, and a geometric albedo at red wavelengths of 0.065 is considered. These values correspond to those determined for comet 67P particles from GIADA (the Grain Impact Analyser and Dust Accumulator, Colangeli et al. 2007) and OSIRIS (the Optical, Spectroscopic and Infrared Remote Imaging System, Keller et al. 2007) measurements on Rosetta spacecraft (Fulle et al. 2016; Fornasier et al. 2015). Further, the particle brightness is corrected for the phase function using a linear phase coefficient of $\phi(\alpha)$=0.03 mag deg^{-1}. This value has been determined for several comets by Meech & Jewitt (1987).

Following a common practice, the particle size distribution is assumed to be described by a power law function, i.e., $n(r) \propto r^{-\kappa}$. The limiting particle sizes, $r_{\rm min}$ and $r_{\rm max}$, are assumed at 5 m and 5 cm, respectively. The value of $r_{\rm min}$ is found after some experimentation with the code. We found that the influence on the tail brightness of particles smaller than that size becomes negligible for the available observations. This result is in line with the findings of Groussin et al. (2019), who determined an excess of 10 m particles compared with submicron ones from the temperature of dust grains in 8P. On the other hand, the maximum radius was set as the order-of-magnitude size of the particles associated with the backscattered signal as detected by radar observations by Harmon et al. (2010), which were of the order of a few centimetres in size. The large upper limit for the particle radius is also justified from observations of the Ursid meteor shower, linked to comet 8P (e.g. Jenniskens et al. 2002). Moreno-Ibanez (2018) analysed several Ursid meteors finding a radius size between 1.7 and 2.4 cm, assuming that they are made of refractory material with a density of 3500 kg m^{-3}. The authors justified that high density by arguing that the particles were emitted from the nucleus a long time ago (several centuries), enough to lose all the volatile material initially contained in them. Assuming that the particles had the same amount of volatile and refractory material when they were released, and that the density was that considered in the present study (800 kg m^{-3}), the initial radius of those particles would be between 3 and 5 cm.

The particle size distribution was assumed constant with the comet heliocentric distance. The value of the power index κ is to be found in the parameter fitting procedure as described below.

The dust velocity after gas decoupling is assumed to follow the typical expression $v(\beta,t) = \beta^\gamma u(t)$, with β standing for the ratio between radiation and gravity forces (equation 1), γ is set to γ=0.5 from gas drag hydrodynamical modelling, and $u(t)$ is a function describing the time evolution of the velocity, which needs to be found from the fitting procedure. The velocity $v(\beta,t)$ is constrained to be larger than the nucleus escape velocity. Groussin et al. (2019) (see also Lamy et al. 2008 and Harmon et al. 2010) derived a bilobated nucleus shape consisting of two contact spheres of radii 2.7 km and

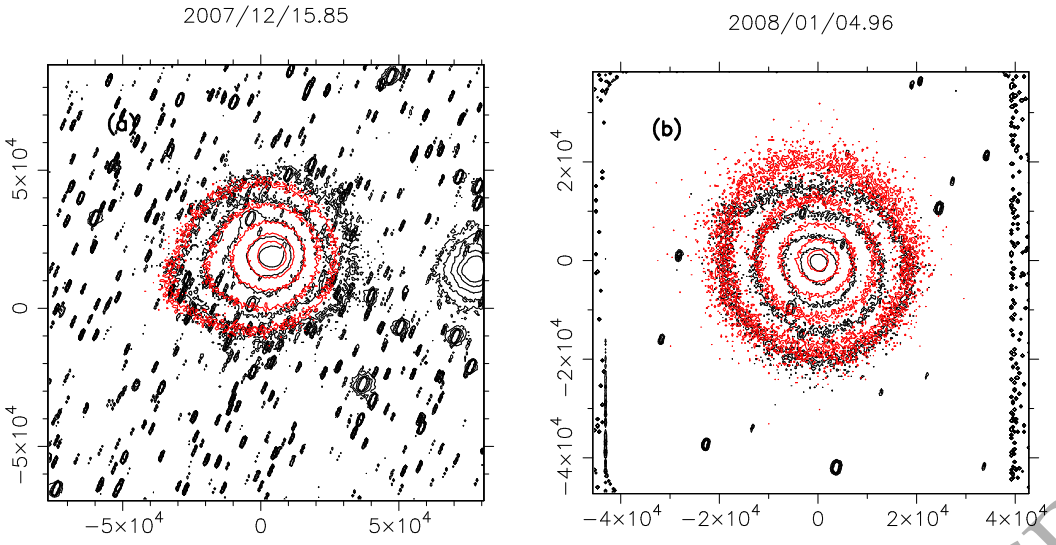

Figure 7. Dust tail brightness of the *R*-band images on the indicated dates. Black contours correspond to the observation and red contours to the dust model. The innermost contours in the left and right panels correspond to 5×10^{-13} and 2×10^{-12} solar disk intensity units, respectively. Contours decrease in brightness in factors of two outwards. The axes are labelled in km projected on the sky. All images are oriented North up, East to the left.

1.1 km. Assuming a reasonable nucleus density of 500 kg m^{-3}, this results in a total mass of M=4.4×10^{13} kg. The size of an equivalent sphere would have a radius of 2760 m, and this results in an escape velocity of v_{esc}=1.46 m s^{-1}. In the simulations concerning the visible data, we added the nucleus brightness to the synthetic dust tails generated. For this purpose, the nucleus is assumed to be a sphere of 2.76 km of radius, having a geometric albedo of 0.065 and a linear phase coefficient of 0.047 mag deg^{-1}, as was found for comet 67P (Fornasier et al. 2015). The effect of the nucleus brightness on the computed synthetic tail images becomes important only for large heliocentric distances. For the simulation of the *Spitzer* image, instead of adding the nucleus contribution, we subtracted the nucleus point spread function profile from the *Spitzer* image, as was estimated by Groussin et al. (2019).

In addition to the time-dependent velocity profile $u(t)$, the dust mass loss rate profile, $dM/dt(t)$, must also be determined from the fitting procedure. We proceeded as follows. We approximate both time-dependent functions by Gaussian profiles. However, asymmetric branches with respect to the maxima have been found in both functions for a wide variety of comets (e.g. Cremonese & Fulle 1994; Fulle et al. 2000; Moreno et al. 2017). In order to account for these asymmetries, we introduce skew parameters. The fitting functions have the general form:

$$f(t) = A \exp \frac{-(t-t_0)^2}{s\sigma^2} \qquad (6)$$

where A is the maximum value of $f(t)$, t_0 is the time of the maximum, σ accounts for the width of the Gaussian, and s is the skew parameter. The nominal Gaussian function has s=1. The Gaussian profile can be skewed to the left or to the right, so we introduce a parameter $s = s_l$ when $t < t_0$, and $s = s_r$ for $t > t_0$. In this way, we can make the profile narrower or broader than the nominal Gaussian, at either side of the maximum, by playing with s_l and s_r (narrower profiles for $s < 1$, and broader profiles for $s > 1$). Since we need the skewed Gaussians for both the dust loss rate and the velocity, this implies eight fitting parameters. The size distribution power index κ completes the set of nine parameters to be found by the multidimensional fitting method. The method used is the downhill simplex described by Nelder & Mead (1965) and is aimed at finding the best-fitting solution to the available observational data, namely, the optical images, the *Spitzer IR*-image, and the Afρ data from the amateur observers. In this regard, it is necessary to point out that Afρ data from the Cometas_obs team between -60 and -20 d from perihelion show a strong discrepancy with the rest of Afρ data (both from the CARA team and from our own analysis, see Fig. 9). Presently, there is no satisfactory explanation for that discrepancy. For that reason, regarding Cometas_obs data, only those between -200 and -60, and between -20 and +150 d from perihelion are considered during the fitting procedure. Data from Cometas_obs between -60 and -20 d from perihelion are disregarded. The best-fitting parameters are found by minimising the squared sum of the differences between the modelled and measured tail brightness and Afρ values. The best-fitting time-dependent dust mass loss rates and velocities (for particles having r=0.1 mm) are shown in Fig. 6. The power law index of the size distribution was found as $\kappa = 3.2 \pm 0.2$. The resulting fits to the *R*-band images and the *Spitzer IR*-image are shown in Figs. 7 and 8, respectively, while the time evolution of the Afρ parameter is depicted in Fig. 9.

5 DISCUSSION

5.1 Comments on the gas results

Fig. 10 shows CN, C_2, C_3, and NH_2 productions rates of 8P estimated by various authors at different pre-perihelion heliocentric distances. Our results for CN, C_2, and C_3, ob-

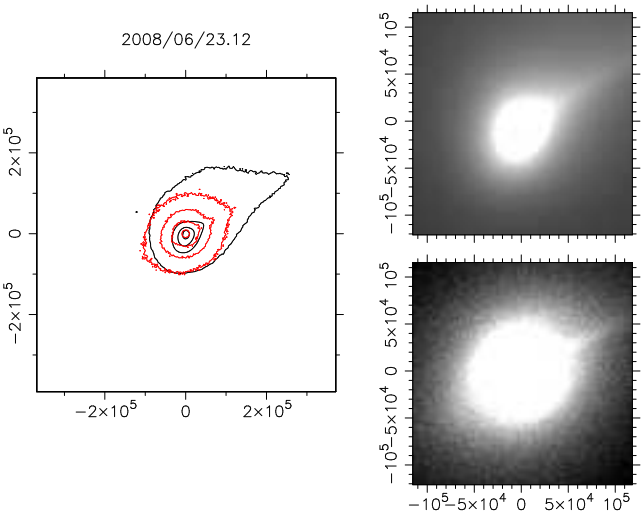

Figure 8. Left panel: Dust tail brightness of the IR *Spitzer*/MIPS image at 24 m. Black contours correspond to the observation and red contours to the dust model. Contours correspond to 80, 50, 35, and 20 MJy sr^{-1}. The upper right and lower right panels are zooms on the observed and modelled tails, respectively, showing the linear condensation to the northwest, which is captured in the dust tail fitting. The axes are labelled in km projected on the sky. North is up, East to the left.

tained at heliocentric distances of 1.21 and 1.08 au pre-perihelion, are compatible with those of Jehin et al. (2009), obtained at perihelion (1.027 au) with a similar procedure, i.e. applying a Haser model and allowing the scale lengths to be different from the customary values to obtain the best-fitting. CN, C_2, and C_3 production rates derived in this work, together with the results by Jehin et al. (2009), suggest a slight increase of activity as the comet approaches perihelion. Our NH_2 estimates also show an increase towards perihelion but, unfortunately, Jehin et al. (2009) did not obtain the NH_2 production rate. By contrast, Borisov et al. (2008), using low-resolution spectra and the scale lengths from A'Hearn et al. (1995), obtained much higher values. Although production rates estimated by different authors or using different techniques frequently show some discrepancies (see e.g. Langland-Shula & Smith 2011), the production rates obtained by Borisov et al. (2008) seem to be very high compared with production rates estimated at nearby heliocentric distances. Transients effects, such as outbursts, cannot be invoked to explain this discrepancy as no event of that type was reported during the continuous observations of the comet in its closest approach to Earth[7]. A similar situation occurs with the production rates obtained at larger pre-perihelion heliocentric distances by Langland-Shula & Smith (2011), being higher than our estimates and those by Jehin et al. (2009).

The results of Schleicher (2007a, 2007b) on CN, C_2, and C_3 at 1.6 and 1.3 au, obtained from narrow-band imaging, are also displayed in Fig. 10. Their results on CN and C_2, together with those of Jehin et al. (2009), and those reported in this work, show an increase of CN and C_2 towards perihelion. C_3 shows a different behaviour. Schleicher (2007b) obtains a C_3 production rate at 1.3 au similar to that obtained by Jehin et al. (2009) at perihelion, suggesting a constant production rate as the comet approaches perihelion. Our C_3 production rate is a factor between 2 and 3 below that level. In principle, that difference cannot be attributed to the fitting procedure and the determination of the scale lengths. That molecule showed little sensitivity to variations in scale lengths, as shown by the small differences between our estimates and the values obtained when the standard scale lengths were used. It is implausible to invoke a change in the composition of the region originating activity as the subsolar point moves towards the north pole (see Fig. 11) affecting just to C_3. Being our data compatible with those of Jehin et al. (2009), currently, we do not have an explanation for the difference with the comparatively high C_3 production rates obtained farther from perihelion.

To compare 8P with other comets, it is convenient to consider the ratios[8] of the different molecules with respect to CN (see Table 4). Regarding the C_2/CN ratio, the previously published results show some discrepancies. On the one hand, Schleicher (2007b) obtained a ratio of 0.17 from observations at 1.3 au, a value that can be considered in agreement with the ratio of 0.11 obtained by Jehin et al. (2009) at perihelion (averaging their productions in the Tail/Sun directions). Both values are in agreement with the estimated one by A'Hearn et al. (1995) at the 1994 perihelion passage, defining 8P as a "typical" comet regarding C_2/CN ratio. On the other hand, Langland-Shula & Smith (2011) obtained a comparatively high ratio of 0.38 (at 1.24 au) while Borisov et al. (2008) reported a C_2/CN ratio of -0.96 (at 1.06 au), a very low value, more typical of comets at large heliocentric distances (A'Hearn et al. 1995).

At 1.21 au (15 December 2007), our nominal C_2/CN ratio (see Table 4) is the same as that of Jehin et al. (2009), and therefore compatible with those obtained by Schleicher (2007b) and A'Hearn et al. (1995). At 1.08 au (4 January 2008), the uncertainly in the C_2/CN ratio is much larger, inherited mainly from the uncertainty in C_2 production rates. Thus, our results for that heliocentric distance cannot be interpreted with confidence.

Considering just the value obtained on 15 December 2007, i.e. 0.11 ± 0.10, it is compatible with the average value for Halley-type comets reported by Cochran et al. (2012), 0.16 ± 0.13, which is also coincident with the average value from their complete set of comets, 0.15 ± 0.20. Therefore, our results support that 8P can be considered as "typical" regarding that ratio.

As in the case of C_2, C_3/CN ratio also shows some discrepancies when comparing previously published values. For this ratio, Schleicher (2007b) obtained an unusually high value of -0.40. That value is much higher than those considered by A'Hearn et al. (1995) as "typical", around -1.0, and also higher than the average value of -0.68 defined by Cochran et al. (2012) from their complete set of comets. At 1.24 au, Langland-Shula & Smith (2011) obtained a ratio of -0.70 and, at perihelion, Jehin et al. (2009) estimated a lower

[7] An almost continuous lightcurve of 8P can be obtained from e.g. http://www.observadores-cometas.com/cometas/8p/lightcurve.html

[8] All daughter production ratios in this section are given as the $\log_{10}$[ratio]

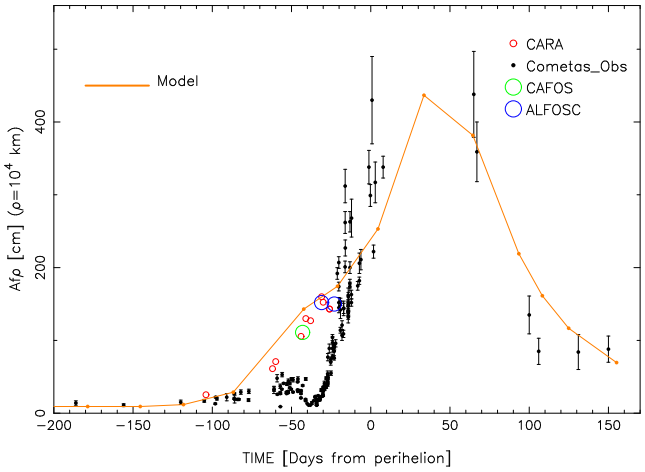

Figure 9. The observed and modelled time dependence of the Afρ parameter, for ρ=10^4 km. Observations include CAFOS and ALFOSC data as well as estimates by the amateur groups CARA and Cometas_Obs. The thick line corresponds to the best-fitting dust tail model result. An important discrepancy in Afρ estimates can be observed when comparing CAFOS, ALFOSC and CARA data with those from Cometas_obs between -60 and -20 d from perihelion. Presently, there is no satisfactory explanation for such discrepancy. Given the consistency between CAFOS, ALFOSC, and CARA data for that range of dates, Cometas_obs data within -60 and -20 d, although shown for completeness, are not considered in the fitting procedure.

value, -1.27. That change would suggest that the C_3 production remained approximately constant while that of CN increased as 8P approached perihelion. Borisov et al. (2008), from their observations at 1.06 au, also obtained a small value for the ratio, -1.04. Our results give a ratio between -1.46 ± 0.09 and -1.31 ± 0.11 for the range 1.21–1.08 au of heliocentric distances, close to the value of Jehin et al. (2009). According to the definition given by Cochran et al. (2012), our estimate for 8P would meet the condition on the C_3/CN ratio to be considered as depleted (log [Q(C_3/Q(CN)] $<$ -0.86). Actually, our ratio is less than the mean value estimated form the sample of depleted comets in Cochran et al. (2012), i.e. -1.06 ± 0.39. The C_2/CN ratio obtained implies that 8P cannot be defined as "depleted" in the strict sense (C_2 and C_3), but our results, supported by those of Jehin et al. (2009), would suggest that 8P is C_3 depleted according to the criterion by Cochran et al. (2012). The situation is different if the dataset by A'Hearn et al. (1995) is considered. A'Hearn et al. (1995, their table 6) provide the range of ratios characterising comets referred to OH (rather than to CN), and the CN/OH ratio slightly depends on the taxonomic class. Schleicher (2007b) found that the CN/OH ratio at 1.3 au was -2.58. Using that value to estimate our C_3/OH ratio, we obtain -4.04 (15 December 2007) and -3.89 (4 January 2008). Both values are within the range of the C_3/OH ratios for "typical" comets, [-4.26,-3.09], according to A'Hearn et al. (1995), if the C_2/CN ratio is higher than -0.18, as in our case. Thus, classification from A'Hearn et al. (1995) allows us to define 8P as a "typical" comet.

Regarding NH_2/CN ratio, Langland-Shula & Smith (2011) obtained a value of 0.95 when the comet was at 1.24 au. Our results, 0.81 ± 0.10 and 0.93 ± 0.11, may be considered in comparatively good agreement with those of Langland-Shula & Smith (2011). Those high values are much larger than the mean value of -0.26 ± 0.40 that Cochran et al. (2012) estimated for 8P from data corresponding to the 1980 perihelion passage. The high values for the NH_2/CN ratio found by Langland-Shula & Smith (2011) and in this study are, in fact, higher than any of the ratios found by Cochran et al. (2012) from their complete dataset. From our results and those of Langland-Shula & Smith (2011), although statistics on NH_2/CN ratio do not allow a meaningful conclusion, 8P would be defined as NH_2 enriched. Interestingly, Cochran et al. (2012) found that Halley-type comets, group to which 8P belongs, showed a slight tendency to enrichment in NH_2 (with a positive average ratio of 0.10 ± 0.34) compared with JFCs (-0.03 ± 0.28) and long-period comets (-0.17 ± 0.22). Therefore, even if 8P is rich in NH_2, this circumstance seems to be common among Halley-type Comets.

Concerning parents molecules, as in Jehin et al. (2009) and Bonev et al. (2008), the scale length measured for CN indicates that HCN cannot be the main parent species. The photodissociation rate of HCN at the comet heliocentric distances ranges from 8.6×10^{-6} to 1.1×10^{-5} s^{-1}, whereas those for CN span from 2.2×10^{-6} to 2.7×10^{-6} s^{-1} (Huebner et al. 1992). Using 0.8 km s^{-1} for the HCN expansion velocity (Fray et al. 2005) and 1 km s^{-1} for the CN ejection velocity, the equivalent parent and daughter scale lengths are in the range of 49 400 – 57 700 km, and 368 000 – 462 000 km, respectively. From the values found in this work (l_p ranging from 27 000 to 63 000 km, and l_d poorly constrained but with values as low as 140000 km), we may conclude that HCN is not the main, or at least the unique, parent of the cyano radical. Other species whose photolysis gives rise to CN are C_2N_2, HC_3N and CH_3CN. The cases of cyanogen and cyanoacetylene as parents of CN would have equivalent parent scale lengths within 20 000 and 32 000 km, shorter than the average value measured in this work, although compatible with our lower limit. Additionally, from our study of the (l_p, l_d, Q) parameter space, we can conclude that both C_2 and C_3 scale lengths (parent and daughter) are larger than customary values. Constraining the CN, C_2, and C_3 parent species requires the development of complex chemical models beyond the scope of this paper.

5.2 Comments on the dust results.

From observations at 1.63 au pre-perihelion (at approximately 87 d before perihelion), Schleicher (2007a) found that, although the daughter molecules abundances of 8P were "typical", the comet showed a very low dust-to-gas ratio. That low ratio was in agreement with estimates at the 1994 perihelion passage obtained by A'Hearn et al. (1995). Schleicher (2007a) concluded that 8P had a very low dust-to-gas ratio based on the quotient Afρ/Q(H_2O), which placed the comet among those with the lowest ratio in the dataset of A'Hearn et al. (1995). Combining our dust mass loss rate with the water production estimated by Schleicher (2007a), a dust-to-water ratio of 0.98 is obtained when the comet was at 1.6 au pre-perihelion, a ratio close to the canonical value of 1. That value seems to indicate that 8P certainly had a low dust-to-water ratio, particularly if compared with the results from Sykes & Walker (1992), who es-

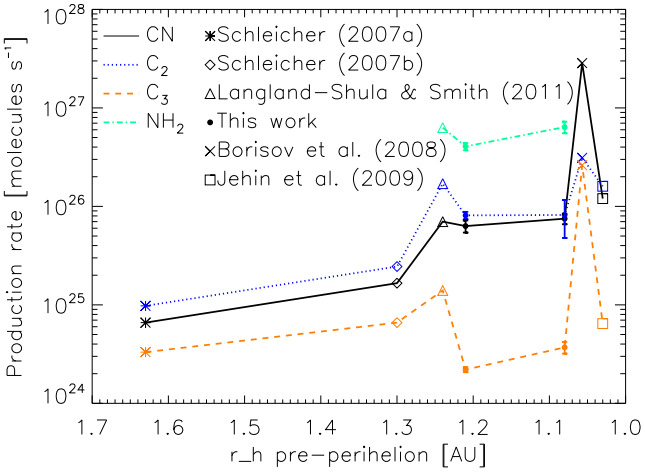

Figure 10. Determinations of CN (black), C_2 (blue), C_3 (orange), and NH_2 (green) production rates of 8P by different authors at different heliocentric distances. Lines joining symbols are intended to guide the eye to connect production rates corresponding to the same molecule.

timated an average dust-to-gas ratio of 3 from the trails of an ensemble of comets, with that of C/1995 O1 (Hale-Bopp) (e.g. Weaver et al. 1999; González et al. 2014) or with that of comet 1P/Halley (e.g. McDonnell et al. 1991; Fulle et al. 2000), among others. Today, it is known that the dust-to-gas ratio varies with heliocentric distance. In fact, as described in the thorough review by Choukroun et al. (2020) as well as in Fulle et al. (2019), estimating the refractory-to-ice, dust-to-gas or dust-to-water ratios is a complex task even in the case of comet 67P/Churyumov-Gerasimenko, for which a wealth of data is available thanks to both Rosetta mission and ground-based observations. Choukroun et al. (2020) estimated the mission integrated dust-to-gas ratio for 67P as 2.3. Nevertheless, this dust-to-gas ratio, which can be considered the best constrained ratio, is affected by a large uncertainty, ranging from 0.64 (Choukroun et al. 2020) up to values as high as 6 (Rotundi et al. 2015), showing a comparatively large variability if estimated from single snapshots at particular heliocentric distances. Fulle et al. (2019) convincingly argued that discrepancies between different estimates of the coma dust-to-gas ratio may converge into a comparatively high value of the nucleus refractory-to-ice ratio if phenomena, such as mass transfer between hemispheres, are considered.

In any case, 8P seems to have a low dust-to-water ratio when estimated from production rates at distances larger than at least 1.6 au pre-perihelion. Nevertheless, from our Monte Carlo modelling of the images of 8P, the dust-to-water ratio increases as the comet approaches perihelion, reaching values between 6 and 11.5, depending on the estimate of the water production rate around perihelion (5.97x 10^{28} molecules s^{-1} by Böhnhardt et al. 2008 or 3.0 x 10^{28} molecules s^{-1} by Kobayashi et al. 2010, obtained just after perihelion at, 1.03 au).

It is worth mentioning that caution is necessary when interpreting the dust content of a comet from Afρ estimates. Certainly, comet 8P, from the Afρ/Q(H_2O) or Afρ/Q(CN) ratios (see Table 4), seems to be among those with the lowest ratios in the dataset by A'Hearn et al. (1995, their fig. 3). If the Afρ at perihelion is considered (approximately 240 cm from Fig. 9) together with the CN production obtained by Jehin et al. (2009), a value of -23.70 is obtained. That value is similar to those in Table 4, indicating little variation of the ratio from 1.21 au up to perihelion. Although the low dust content of the coma derived from Afρ is consistent with our modelling at large heliocentric distances, estimates based on Afρ close to perihelion show conflicting results when compared to those obtained using Monte Carlo modelling. In this regard, it is necessary to realise that Afρ is proportional to the dust loss rate times the cross section of the dust grains divided by the mean dust velocity of the observed grains (Fulle 2000).

The increase of the dust-to-water ratio is mainly due to the relative increase of the dust mass ejection. Indeed, while water production increases by a factor between 7.5 and 15 from 1.6 au up to perihelion, dust ejected mass increases by a factor approximately an order of magnitude larger. After perihelion, dust mass ejection decreases much faster than water production. At 2.24 au post-perihelion, considering the water production estimated by Groussin et al. (2019), the dust-to-water ratio is only 0.20. Thus, the dust mass loss rate obtained from the Monte Carlo dust tail modelling, together with the water production rates available from different observations, indicates that comet 8P shows a coma with a comparatively low dust-to-water ratio at large heliocentric distances. By contrast, close to perihelion, the ratio reaches values that can be considered high, between 6 and 12. These high values are in line with those considered by Fulle et al. (2000) to analyse 1P/Halley data from *Giotto* (ESA) and with the ratios found for comet C/1995 O1 (Hale-Bopp) (see e.g. González et al. 2014, their fig. 1). Unfortunately, available water production rates do not allow us to integrate the productions to give an average value for the coma dust-to-water ratio. In any case, given the behaviour of the comet near perihelion, it cannot be concluded that 8P has a low dust-to-water ratio. The ratio reaches values that can be described as "typical". It is necessary to notice that the ratios found in this study may be considered as lower limits if the nucleus emits particles larger than 5 cm. Very large particles would contribute efficiently to the total mass loss, but their effect on the coma brightness would be comparatively small, making it difficult to assess their contribution with the dust model.

Fig. 6 shows that peaks of particles velocity and dust production do not occur at the same time. While particle velocity peaks at perihelion, dust loss rate peaks approximately 20-25 days after. Interestingly, the same behaviour was found for comet 67P (Moreno et al. 2017). Dust production curve and asymmetry resemble those of the subsolar latitude for the spin axis determined by Groussin et al. (2019), that is (RA, Dec) = $(285 \pm 12, +20 \pm 5)^\circ$. For that pole solution, subsolar latitude is -40° at -200 d from perihelion, reaches the northward equinox at -73 d, and peaks at +80° two weeks after perihelion. Fig. 11 displays the dust mass production rate as a function of the subsolar latitude, clearly showing a correlation between both quantities. In principle, that figure may suggest different activity characteristics for both hemispheres of 8P, as was the case for 67P. As it is known, the northern hemisphere of 67P was fed with icy particles that fell from those released from the southern hemisphere when it was illuminated at perihelion

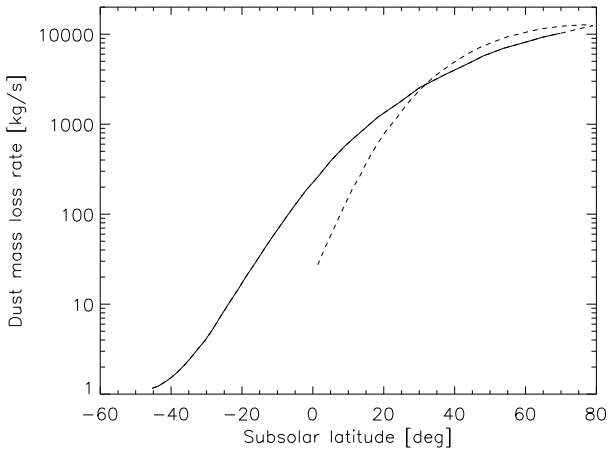

Figure 11. Dust mass loss rate as a function of the subsolar latitude determined from the pole solution obtained by Groussin et al. (2019). Solid and dashed lines correspond to the pre-perihelion and post-perihelion branches of the orbit, respectively.

(e.g. Thomas et al. 2015; Pajola et al. 2019; Davidsson et al. 2021). As Fulle et al. (2017) pointed out, mass transfer may apply to all comets because the asymmetric gas density cannot prevent "airfall"[9]. This would be particularly true for comets with strong seasonal effects, as 8P with the spin axis inclination determined by Groussin et al. (2019). Indeed, Schleicher & Bair (2008) already pointed out that 8P could be affected by significant seasonal effects. The main difference between 67P and 8P is that, given the different arguments of their spin axes, in the latter comet the northern hemisphere would be the producer of material falling back onto the southern hemisphere.

Leaving aside the mass transfer as a process contributing to the seasonal dependence of the activity, other factors may also have contributed to the increased dust mass ejection when the subsolar latitude moves across the surface of the nucleus. For example, the activation of new source regions (as Schleicher & Bair 2008 suggested) or increased sublimation in a permanently illuminated polar region.

Another quantity that may show seasonal dependence is the slope of the dust size distribution (κ index). Comet 67P showed a transition from a slope of 3 when the northern hemisphere was illuminated to a steeper one, between 3.6 and 4.3, when the illumination was over the southern hemisphere (e.g. Della Corte et al. 2016; Moreno et al. 2017). Regarding 8P, given the potentially high spin axis inclination, its coma could also hide a strong seasonal variation of the dust size distribution. Unfortunately, the scarcity of available observations, particularly imaging data, prevents us from performing a more complete analysis, including time-dependent size distribution functions. The slope of the size distribution found for 8P, i.e. 3.2 ± 0.2, can be considered as "typical" among comets, with 3.3 ± 0.2 being the average value obtained from inverse tail models (Fulle et al. 1995). Given the comparatively small slope found with our procedure, most of the dust mass in the perihelion coma of 8P is released in the form of large grains.

6 SUMMARY AND CONCLUSIONS

Comet 8P/Tuttle, selected as a possible backup target for the *Comet Interceptor* mission, was observed during its previous perihelion passage to obtain visible images and low-resolution spectra. Observations were performed when the comet was between 1.21 and 1.08 au from the Sun pre-perihelion, during its close approach to Earth in 2007–2008. These data help fill the gap between similar previously reported observations (e.g. Jehin et al. 2009; Schleicher 2007a; Borisov et al. 2008)

Low-resolution spectra were used to estimate CN, C_2, C_3, and NH_2 production rates. From our estimates and the corresponding ratios, we conclude that 8P can be defined as "typical" regarding C_2 and C_3 according to A'Hearn et al. (1995) taxonomic classification. Under Cochran et al. (2012) criteria, 8P is found to be C_3 depleted, although it cannot be defined as a "depleted" comet in the strict sense because it does not meet the C_2 condition. Regarding NH_2, 8P could be considered, as found for other Halley-type Comets, NH_2 enriched according to the statistics of Cochran et al. (2012)

Our visible images, together with infrared images available at the *Spitzer Heritage Archive* corresponding to the program lead by O. Groussin (Groussin et al. 2019) and the Afρ estimates by both CARA and Cometas_Obs amateur teams, have been analysed by using a Monte Carlo dust tail model. From this analysis, it has been obtained that 8P/Tuttle has a dust size distribution characterised by a slope of 3.2 ± 0.2, a value that can be considered "typical" among those retrieved using the same technique. Combining the dust loss rate obtained in this study with available water production rates, it is obtained that the dust-to-gas ratio increases from comparatively low values when the comet is at 1.6 au pre-perihelion up to values above 6 when the comet is at perihelion. After perihelion, the dust-to-water ratio decreases again, reaching values as low as 0.2 at 2.24 au post-perihelion. The significant increase observed in the coma dust-to-water ratio may be a consequence of the high inclination of the spin axis, favouring the existence of a region quasi permanently illuminated when the comet approaches the Sun. Seasonal mass transfer between hemispheres may also contribute to the evolution of the dust-to-water ratio over time. Our results at large heliocentric pre-perihelion distances confirm those obtained by Schleicher (2007a), defining the coma of 8P as one with a low dust-to-water ratio. Nevertheless, as the comet approaches the Sun, the coma dust-to-water ratio increases up to values that can be considered "typical". A high refractory-to-ice ratio would characterise the nucleus of 8P if, as Fulle et al. (2019) pointed out, that ratio is an order of magnitude larger than that estimated from the coma.

One of the 8P most noticeable characteristics may be the high inclination of its spin axis if the determination by Groussin et al. (2019) is confirmed. That high inclination would bring the nucleus under strong seasonal effects worth studying to continue learning on the development of cometary activity. Should this comet be finally selected as backup target for the *Comet Interceptor* mission, we think

[9] Here, we use the term 'airfall" with the meaning originally given by Thomas et al. (2015)

that an encounter at the pre-perihelion equinox would be very valuable, and at the same time still safe, to contribute to our understanding of cometary activity.

ACKNOWLEDGEMENTS

We are very grateful to an anonymous referee for appropriate and constructive comments. The data presented here were obtained in part with ALFOSC, which is provided by the Instituto de Astrofísica de Andalucía (IAA) under a joint agreement with the University of Copenhagen and NOTSA. The research is also based on observations collected at the Centro Astronómico Hispano-Alemán (CAHA) at Calar Alto, operated jointly by Junta de Andalucía and Consejo Superior de Investigaciones Científicas (IAA-CSIC). This work is based in part on observations from the program ID 40270 (PI: O. Groussin) DS_IDENT: ads/sa.spitzer#0024069632 made with the *Spitzer Space Telescope*, which was operated by the Jet Propulsion Laboratory, California Institute of Technology under a contract with NASA. The authors deeply acknowledge the priceless effort performed by both CARA (http://cara.uai.it/ and in particular to LIG02, Rolando Ligustri) and the Cometas_obs team (http://www.astrosurf.com/cometas-obs/, and in particular to Julio Castellano and Esteban Reina for sending the complete dataset) in systematically observing comets and for making available to the community their very valuable estimates. The authors acknowledge financial support from the State Agency for Research of the Spanish MCIU through the "Centre of Excellence Severo Ochoa" award to the Instituto de Astrofísica de Andalucía (SEV-2017-0709). LML and PJG acknowledge funding from project PGC2018-099425-B-I00 (MCI/AEI/FEDER, UE). FM acknowledges support from projects P18-RT-1854 (Junta de Andalucía) and RTI-2018-095330-B-100 (MCIU). This work has made use of NASA's Astrophysics Data System Bibliographic Services and of the JPL's Horizons system.

DATA AVAILABILITY

The data underlying this article will be shared on reasonable request to the corresponding author.

REFERENCES

A'Hearn M. F., Millis R. C., Schleicher D. O., Osip D. J., Birch P. V., 1995, Icarus, 118, 223
Barber R. J., Miller S., Dello Russo N., Mumma M. J., Tennyson J., Guio P., 2009, MNRAS, 398, 1593
Bertini I., Lara L. M., Vincent J. B., Boehnhardt H., Küppers M., Rodrigo R., 2009, A&A, 496, 235
Biver N., et al., 2008, in Asteroids, Comets, Meteors 2008. p. 8151
Bockelée-Morvan D., et al., 2008, in Asteroids, Comets, Meteors 2008. p. 8190
Böhnhardt H., Mumma M. J., Villanueva G. L., DiSanti M. A., Bonev B. P., Lippi M., Käufl H. U., 2008, ApJ, 683, L71
Bonev B. P., Mumma M. J., Radeva Y. L., DiSanti M. A., Gibb E. L., Villanueva G. L., 2008, ApJ, 680, L61
Borisov G., Waniak W., Bonev T., Czart K., Drahus M., 2008, Bulgarian Astronomical Journal, 10, 59
Carusi A., Valsecchi G. B., 1987, Publications of the Astronomical Institute of the Czechoslovak Academy of Sciences, 2, 21
Choukroun M., et al., 2020, Space Sci. Rev., 216, 44
Cochran A. L., Barker E. S., Ramseyer T. F., Storrs A. D., 1992, Icarus, 98, 151
Cochran A. L., Barker E. S., Gray C. L., 2012, Icarus, 218, 144
Colangeli L., et al., 2007, Space Sci. Rev., 128, 803
Cremonese G., Fulle M., 1994, Planet. Space Sci., 42, 263
Crovisier J., Colom P., Biver N., Bockelée-Morvan D., 2008, in Asteroids, Comets, Meteors 2008. p. 8119
Davidsson B. J. R., et al., 2021, Icarus, 354, 114004
Della Corte V., et al., 2016, MNRAS, 462, S210
Fornasier S., et al., 2015, A&A, 583, A30
Fray N., Bénilan Y., Cottin H., Gazeau M. C., Crovisier J., 2005, Planet. Space Sci., 53, 1243
Fulle M., 1989, A&A, 217, 283
Fulle M., 2000, Icarus, 145, 239
Fulle M., Colangeli L., Mennella V., Rotundi A., Bussoletti E., 1995, A&A, 304, 622
Fulle M., Levasseur-Regourd A. C., McBride N., Hadamcik E., 2000, AJ, 119, 1968
Fulle M., et al., 2016, MNRAS, 462, S132
Fulle M., et al., 2017, MNRAS, 469, S45
Fulle M., et al., 2019, MNRAS, 482, 3326
González M., Gutiérrez P. J., Lara L. M., 2014, A&A, 563, A98
Groussin O., Lamy P. L., Kelley M. S. P., Toth I., Jorda L., Fernández Y. R., Weaver H. A., 2019, A&A, 632, A104
Harmon J. K., Nolan M. C., Howell E. S., Giorgini J. D., Magri C., 2008a, in AAS/Division for Planetary Sciences Meeting Abstracts #40. p. 5.01
Harmon J. K., Nolan M. C., Howell E. S., Giorgini J. D., 2008b, in Asteroids, Comets, Meteors 2008. p. 8025
Harmon J. K., Nolan M. C., Howell E. S., Giorgini J. D., 2008c, IAU Circ., 8909, 1
Harmon J. K., Nolan M. C., Giorgini J. D., Howell E. S., 2010, Icarus, 207, 499
Haser L., 1957, Bulletin de la Societe Royale des Sciences de Liege, 43, 740
Huebner W. F., Keady J. J., Lyon S. P., 1992, Ap&SS, 195, 1
Jehin E., et al., 2009, Earth Moon and Planets, 105, 343
Jenniskens P., et al., 2002, Icarus, 159, 197
Keller H. U., et al., 2007, Space Sci. Rev., 128, 433
Kobayashi H., et al., 2010, A&A, 509, A80
Lamy P. L., Toth I., Jorda L., Weaver H. A., Groussin O., A'Hearn M. F., 2008, in AAS/Division for Planetary Sciences Meeting Abstracts #40. p. 5.02
Langland-Shula L. E., Smith G. H., 2011, Icarus, 213, 280
Lara L. M., Schulz R., Stüwe J. A., Tozzi G. P., 2001, Icarus, 150, 124
Lara L. M., Rodrigo R., Tozzi G. P., Boehnhardt H., Leisy P., 2004a, A&A, 420, 371
Lara L. M., Tozzi G. P., Boehnhardt H., DiMartino M., Schulz R., 2004b, A&A, 422, 717
Levison H. F., 1996, in Rettig T., Hahn J. M., eds, Astronomical Society of the Pacific Conference Series Vol. 107, Completing the Inventory of the Solar System. pp 173–191
Levison H. F., Duncan M. J., 1994, Icarus, 108, 18
Licandro J., Tancredi G., Lindgren M., Rickman H., Hutton R. G., 2000, Icarus, 147, 161
Lippi M., Boehnhardt H., Mumma M. J., Villanueva G. L., Disanti M. A., Bonev B., 2009, in European Planetary Science Congress 2009. p. 208
Lovell A. J., Howell E. S., 2008, in Asteroids, Comets, Meteors 2008. p. 8379
McDonnell J. A. M., Lamy P. L., Pankiewicz G. S., 1991, Physical Properties of Cometary Dust. IAU Colloq. 116: Comets in the post-Halley era. p. 1043
Meech K. J., Jewitt D. C., 1987, A&A, 187, 585

Moreno-Ibanez M., 2018, PhD thesis, Universitat Autònoma de Barcelona.
Moreno F., Pozuelos F., Aceituno F., Casanova V., Sota A., Castellano J., Reina E., 2012, ApJ, 752, 136
Moreno F., et al., 2016, A&A, 587, A155
Moreno F., et al., 2017, MNRAS, 469, S186
Moreno F., et al., 2019, A&A, 624, L14
Nelder J. A., Mead R., 1965, Computer Journal, 7, 308
Pajola M., et al., 2019, MNRAS, 485, 2139
Rauer H., et al., 2003, A&A, 397, 1109
Rotundi A., et al., 2015, Science, 347, aaa3905
Schleicher D., 2007a, Central Bureau Electronic Telegrams, 1113, 1
Schleicher D., 2007b, IAU Circ., 8903, 2
Schleicher D. G., 2010, AJ, 140, 973
Schleicher D. G., Bair A. N., 2008, in AAS/Division for Planetary Sciences Meeting Abstracts #40. p. 16.20
Schulz R., Arpigny C., Manfroid J., Stuewe J. A., Tozzi G. P., Cremonese G., Rembor K., Peschke S., 1998, A&A, 335, L46
Schwamb M. E., Knight M. M., Jones G. H., Snodgrass C., Bucci L., Sánchez Pérez J. M., Skuppin N., Comet Interceptor Science Team 2020, Research Notes of the American Astronomical Society, 4, 21
Snodgrass C., Jones G. H., 2019, Nature Communications, 10, 5418
Snodgrass C., Lowry S. C., Fitzsimmons A., 2008, MNRAS, 385, 737
Sykes M. V., Walker R. G., 1992, Icarus, 95, 180
Thomas N., et al., 2015, A&A, 583, A17
Waniak W., Borisov G., Drahus M., Bonev T., Czart K., Küppers M., 2009, Earth Moon and Planets, 105, 327
Weaver H. A., Feldman P. D., A'Hearn M. F., Arpigny C., Brandt J. C., Stern S. A., 1999, Icarus, 141, 1
Weissman P. R., Choi Y. J., Lowry S. C., 2008, in AAS/Division for Planetary Sciences Meeting Abstracts #40. p. 2.03
Woodney L., Schleicher D. G., Bair A. N., 2008, in AAS/Division for Planetary Sciences Meeting Abstracts #40. p. 16.21
de León J., et al., 2020, MNRAS, 495, 2053

This paper has been typeset from a TEX/LATEX file prepared by the author.